

# Investigation of the $e^+e^- \rightarrow \omega\pi^0 \rightarrow \pi^0\pi^0\gamma$ reaction in the energy domain near the $\phi$ -meson

M. N. Achasov, V. M. Aulchenko, A. V. Berdyugin, A. V. Bozhenok,  
 D. A. Bukin, S. V. Burdin, T. V. Dimova, V. P. Druzhinin,  
 M. S. Dubrovin, I. A. Gaponenko, V. B. Golubev, V. N. Ivanchenko,  
 I. A. Koop, A. A. Korol, S. V. Koshuba, E. V. Pakhtusova,  
 A. A. Salnikov, V. V. Shary, S. I. Serednyakov, Yu. M. Shatunov,  
 V. A. Sidorov, Z. K. Silagadze \*, A. A. Valishev

Budker Institute of Nuclear Physics, 630 090, Novosibirsk, Russia  
 Novosibirsk State University, 630 090, Novosibirsk, Russia

## Abstract

The  $e^+e^- \rightarrow \omega\pi^0 \rightarrow \pi^0\pi^0\gamma$  process was investigated in the SND experiment at the VEPP-2M collider. A narrow energy interval near the  $\phi$ -meson was scanned. The observed cross-section reveals, at the level of three standard deviation, the interference effect caused by  $\phi \rightarrow \pi^0\pi^0\gamma$  decay. The cross-section parameters, as well as the real and imaginary parts of the  $\phi$ -meson related amplitude, were measured.

## 1 Introduction

There are several reasons [1, 2], which make the experimental study of the  $e^+e^- \rightarrow \omega\pi^0$  reaction interesting. First of all, it is expected that the radial excitations of  $\rho$ -meson should reveal themselves in this process, thus giving us a possibility to study their properties. The  $e^+e^- \rightarrow \omega\pi^0$  transition is also important for the precise determination of the total cross section of  $e^+e^-$  annihilation into hadrons. In the vector meson dominance model  $e^+e^- \rightarrow \omega\pi^0$  transition is connected to the  $\omega\rho\pi$  vertex, which appears also in a number of hadron decays, like  $\omega \rightarrow 3\pi$ ,  $\omega \rightarrow \pi^0\gamma$ ,  $\rho \rightarrow \pi\gamma$ ,  $\omega \rightarrow \mu^+\mu^-\pi^0$ ,  $\pi^0 \rightarrow 2\gamma$ . The precise experimental data about these processes stimulate theoretical study of the underlying hadron dynamics. In the low energy limit, the chiral perturbation theory [3] and effective chiral Lagrangians [4]

---

\*Corresponding author. Fax +7 3832 34 21 63, e-mail silagadze@inp.nsk.su

give a phenomenological description of meson physics, as it is commonly believed nowadays. But their applicability is in question for energies above 1 GeV. On the other hand, for energies  $1 \div 2$  GeV, the perturbative QCD is also not applicable. So any precise experimental information in this energy range can be considered as "data in searching of the theory". Simple but successful vector meson dominance picture may become insufficient when the precision of the data increases.

The  $e^+e^- \rightarrow \omega\pi^0$  transition can be studied in either  $e^+e^- \rightarrow \omega\pi^0 \rightarrow \pi^+\pi^-\pi^0\pi^0$  or  $e^+e^- \rightarrow \omega\pi^0 \rightarrow \pi^0\pi^0\gamma$  channels. The former can provide about one order of magnitude more statistics, but the latter is more preferable concerning background conditions.

The  $e^+e^- \rightarrow \omega\pi^0 \rightarrow \pi^0\pi^0\gamma$  reaction was studied earlier in the energy range  $1.0 \div 1.4$  GeV by the ND detector [1, 2]. Indirectly, the  $\sigma(e^+e^- \rightarrow \omega\pi^0)$  cross section was extracted also from the ARGUS data on  $\tau^- \rightarrow \nu_\tau\omega\pi^-$  decay [5], under assumption of the Conserved Vector Current (CVC). The results are in good agreement, thus confirming the CVC hypothesis [6].

In 1995 a new set of experiments began with the SND detector [7, 8, 9] on the Novosibirsk VEPP-2M storage ring [10]. The maximum luminosity of VEPP-2M at  $2E = 1\text{GeV}$  equals  $3 \cdot 10^{30} \text{cm}^{-2} \text{sec}^{-1}$ .

Below we report the results on  $e^+e^- \rightarrow \omega\pi^0 \rightarrow \pi^0\pi^0\gamma$  process, based on 1996-1997 two-year SND statistics. In 1996 several scans were made of the energy interval  $2E = 984 \div 1040\text{MeV}$  [11]. From the 1997 experiment [12] a part of statistics, collected at the center of mass energies 980, 1040 and 1060 MeV, was used.

## 2 Theoretical Model

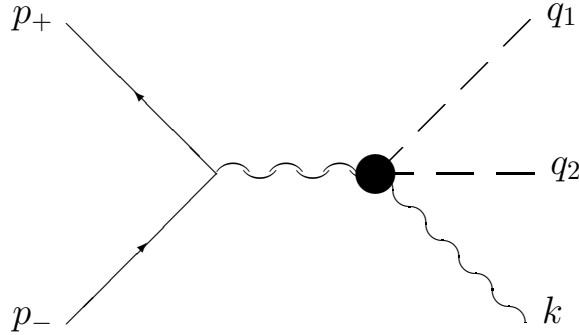
As we have already mentioned in the introduction, currently no definite predictions can be made from the basic first-principle theory of strong interactions (QCD) in this energy range. The limited accuracy of the existing experimental data leaves enough room for various phenomenologically inspired models. Now a light is seen at the end of the tunnel: several meson factories come into operation, and also a new generation of fixed-target experiments will accumulate a huge number of events with strongly interacting particles. So the experimental information is expected to become increasingly precise. Of course a common wisdom says that "If we see a light at the end of the tunnel, it's the light of an oncoming train" [13]. So

it is not excluded that the present theoretical models will be shattered by this “train”, but it can deliver a new passenger also.

Here we consider a simple phenomenological model, based on the vector meson dominance scheme. Our aim is twofold: to estimate the expected cross section and to establish a framework for Monte-Carlo simulation.

## 2.1 General considerations

Let  $J_\mu$  be the matrix element of the electromagnetic current between the vacuum and the  $\pi^0\pi^0\gamma$  final state. Then the amplitude for the  $e^+e^- \rightarrow \pi^0\pi^0\gamma$  transition via one-photon annihilation diagram



reads (up to irrelevant phase factor)

$$M(e^+e^- \rightarrow \pi^0\pi^0\gamma) = \frac{e}{s} \bar{v}(p_+) \gamma_\mu u(p_-) J^\mu, \quad s = (p_+ + p_-)^2.$$

The standard considerations lead to the following cross section with unpolarized beams [14]

$$d\sigma(e^+e^- \rightarrow \pi^0\pi^0\gamma) = \frac{\pi\alpha}{s^2} (\overline{J_1^* \cdot J_1} + \overline{J_2^* \cdot J_2}) d\Phi, \quad (1)$$

where only transverse (with respect to the beam direction) components of  $\vec{J}$  contribute and the invariant phase space element is

$$d\Phi = \frac{d\vec{q}_1}{(2\pi)^3 2E_1} \frac{d\vec{q}_2}{(2\pi)^3 2E_2} \frac{d\vec{k}}{(2\pi)^3 2\omega} (2\pi)^4 \delta(Q - q_1 - q_2 - k).$$

$J_\mu$  should satisfy the current conservation condition  $Q_\mu J^\mu = 0$ . On the other hand  $J_\mu = T_{\mu\nu} \epsilon^\nu$ ,  $\epsilon^\nu$  being the photon polarization 4-vector. So  $T_{\mu\nu}$  is a gauge invariant tensor:

$$Q_\mu T^{\mu\nu} = k_\nu T^{\mu\nu} = 0.$$

There exists a general procedure how to construct such gauge invariant tensors which are free from kinematical singularities [15]. In our case there are just three independent tensors [16]

$$\begin{aligned} L_{\mu\nu}^{(1)} &= (k \cdot Q)g_{\mu\nu} - k_\mu Q_\nu, \quad Q = q_1 + q_2 + k = p_- + p_+, \quad q = \frac{1}{2}(q_1 - q_2) \\ L_{\mu\nu}^{(2)} &= (k \cdot Q)q_\mu q_\nu - (k \cdot q)(k_\mu q_\nu + q_\mu Q_\nu) + (k \cdot q)^2 g_{\mu\nu} \\ L_{\mu\nu}^{(3)} &= (k \cdot q)[Q^2 g_{\mu\nu} - Q_\mu Q_\nu] + q_\nu[(k \cdot Q)Q_\mu - Q^2 k_\mu]. \end{aligned}$$

So

$$T_{\mu\nu} = \frac{A_1}{E^2} L_{\mu\nu}^{(1)} + \frac{A_2}{E^4} L_{\mu\nu}^{(2)} + \frac{A_3}{E^4} L_{\mu\nu}^{(3)}.$$

dimensionless form factors  $A_i$  are determined by the concrete dynamical model. Summing over the final state photon polarizations (REDUCE program [17] proves to be useful for these calculations) and performing the angular integration, we get [16]

$$\begin{aligned} \frac{1}{4}(\overline{J_1^* \cdot J_1} + \overline{J_2^* \cdot J_2}) &= -\frac{1}{4}(T_1^{\nu*} T_{1\nu} + T_2^{\nu*} T_{2\nu}) \longrightarrow F(x, x_1, x_2) = \\ C_{11}|A_1|^2 + C_{22}|A_2|^2 + C_{33}|A_3|^2 + C_{12}(A_1 A_2^* + A_1^* A_2) + & \quad (2) \\ C_{13}(A_1 A_3^* + A_1^* A_3) + C_{23}(A_2 A_3^* + A_2^* A_3), & \end{aligned}$$

where ( $x = \frac{\omega}{E} = 2 - x_1 - x_2$ ,  $x_i = \frac{E_i}{E}$ ,  $r = \frac{m_\pi}{E}$ )

$$\begin{aligned} C_{11} &= \frac{4}{3}x^2, \quad C_{13} = \frac{8}{3}x(x_1 - x_2), \quad C_{23} = \frac{4}{3}(x_1 - x_2)^3, \\ C_{22} &= \frac{1}{3}(x_1 - x_2)^4 + \frac{2}{3}x^2(r^2 - 1 + x)^2 + \frac{2}{3}(x_1 - x_2)^2(1 - x)(r^2 - 1 + x) \\ C_{33} &= \frac{8}{3}(x_1 - x_2)^2(1 + x) - \frac{8}{3}x^2(r^2 - 1 + x) \quad (3) \\ C_{12} &= \frac{2}{3}[(x_1 - x_2)^2 + x^2(r^2 - 1 + x)]. \end{aligned}$$

So for the total cross-section we obtain (the factor  $\frac{1}{2}$  accounts for identical  $\pi^0, s$ )

$$\begin{aligned} \sigma(e^+ e^- \rightarrow \pi^0 \pi^0 \gamma) &= \frac{\alpha}{256\pi^2 E^2} \int_{x_{1-}}^{x_{1+}} dx_1 \int_{x_{2-}}^{x_{2+}} dx_2 F(2 - x_1 - x_2, x_1, x_2) \\ &= \frac{\alpha}{256\pi^2 E^2} \int_{x_-}^{x_+} dx \int_{x_{2-}^*}^{x_{2+}^*} dx_2 F(x, 2 - x - x_2, x_2). \quad (4) \end{aligned}$$

The integration limits are determined from the condition

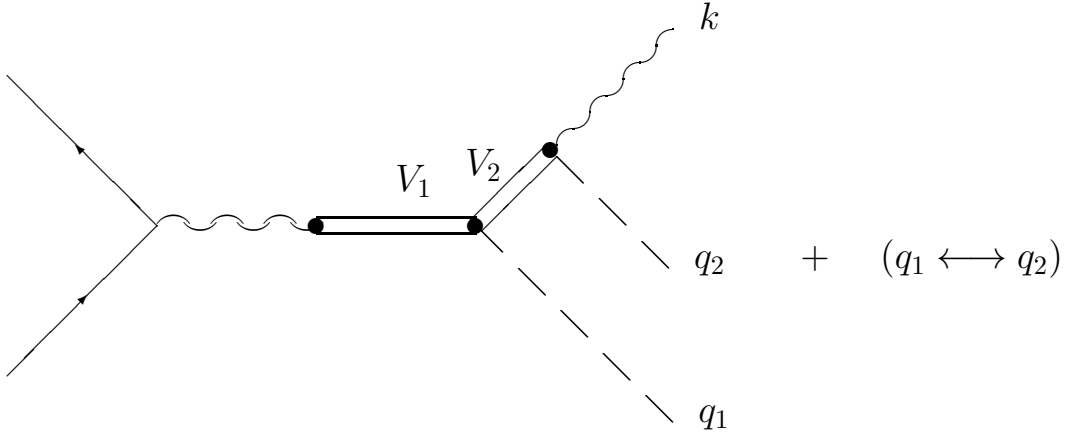
$$|\cos \theta_{12}| = \left| \frac{(2E - E_1 - E_2)^2 - \vec{q}_1^2 - \vec{q}_2^2}{2|\vec{q}_1||\vec{q}_2|} \right| \leq 1 ,$$

which gives

$$\begin{aligned} x_{1-} &= r , \quad x_{1+} = 1 , \quad x_- = 0 , \quad x_+ = 1 - r^2 , \\ x_{2\pm} &= \frac{1}{1 - x_1 + \frac{r^2}{4}} \left\{ \left(1 - \frac{x_1}{2}\right) \left(1 - x_1 + \frac{r^2}{2}\right) \pm \right. \\ &\quad \left. \frac{1}{2}(1 - x_1)\sqrt{x_1^2 - r^2} \right\} , \quad x_{2\pm}^* = 1 + \frac{x}{2} \left[ -1 \pm \sqrt{\frac{1 - r^2 - x}{1 - x}} \right] . \end{aligned} \quad (5)$$

## 2.2 Vector mesons contribution

To proceed, we need expressions for the  $A_i$  form factors. It is expected that the main contribution comes from diagrams of the following type



Using kinematical structures of the  $V_1 \rightarrow V_2\pi^0$  and  $V \rightarrow \pi^0\gamma$  vertexes, which are determined from the Lorentz covariance, we get for the form factors [16]

$$\begin{aligned} A_1 &= -\frac{1}{4} \left( \frac{m^2}{E^2} - 1 + \frac{3}{2}x \right) [g(x_1) + g(x_2)] + \frac{1}{4}(x_1 - x_2)[g(x_1) - g(x_2)], \\ A_2 &= \frac{1}{4}[g(x_1) + g(x_2)] , \quad A_3 = -\frac{1}{8}[g(x_1) - g(x_2)] , \end{aligned} \quad (6)$$

where

$$g(x) = \sum_{V_1, V_2 = \rho, \omega, \phi} g^{(V_1, V_2)}(x) ,$$

and individual contributions look like (note that  $V \rightarrow \pi\gamma$  coupling constant is defined as  $eg_{V\pi\gamma}$ )

$$g^{(V_1, V_2)}(x) = \pi\alpha M_{V_1}^2 \frac{g_{V_1 V_2 \pi} g_{V_2 \pi \gamma}}{g_{V_1}} \frac{s}{s - M_{V_1}^2 + iM_{V_1}\Gamma_{V_1}} \frac{1}{1 - x + \gamma_{V_2}},$$

$$\gamma_V = \frac{1}{s}(m^2 - M_V^2 + iM_V\Gamma_V). \quad (7)$$

To take into account the resonance width dependence on energy, one should replace  $M_V\Gamma_V \rightarrow \sqrt{q^2}\Gamma_V(q^2)$ ,  $q$  being the resonance 4-momentum.

### 2.3 Coupling constants

$g_{V\pi\gamma}$  can be determined from the  $V \rightarrow \pi^0\gamma$  decay width. Namely

$$g_{V\pi\gamma}^2 = \frac{24 M_V^3 \Gamma(V \rightarrow \pi^0\gamma)}{\alpha (M_V^2 - m_\pi^2)^3}.$$

Using  $\Gamma(\omega \rightarrow \pi^0\gamma)$ ,  $\Gamma(\rho^+ \rightarrow \pi^+\gamma)$ , and  $\Gamma(\phi \rightarrow \pi^0\gamma)$  as inputs, we get

$$g_{\omega\pi\gamma} = (2.32 \pm 0.06)\text{GeV}^{-1}, \quad g_{\rho\pi\gamma} = (0.73 \pm 0.04)\text{GeV}^{-1},$$

$$g_{\phi\pi\gamma} = (0.138 \pm 0.007)\text{GeV}^{-1}. \quad (8)$$

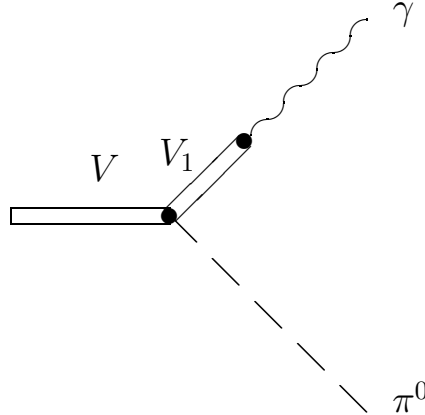
As for the photon–vector meson coupling constant, it can be determined from the  $\Gamma(V \rightarrow e^+e^-)$  width

$$\frac{g_V^2}{4\pi} = \frac{\alpha^2 M_V}{3 \Gamma(V \rightarrow e^+e^-)},$$

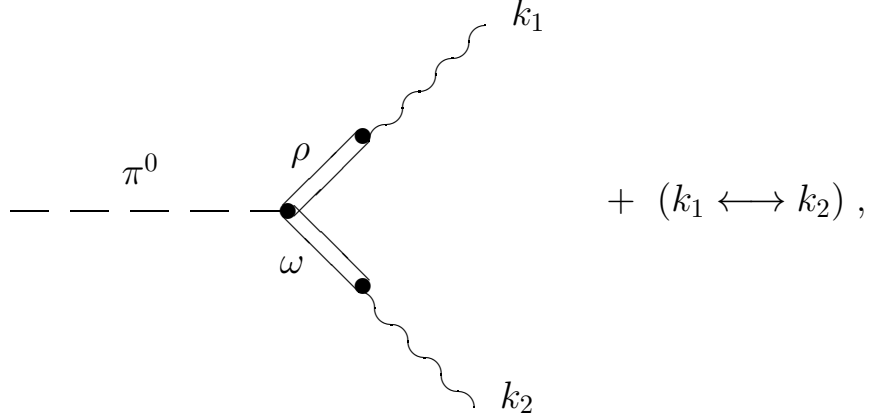
and we get

$$g_\rho = 5.0 \pm 0.1, \quad g_\omega = 17.0 \pm 0.3, \quad g_\phi = 12.9 \pm 0.2. \quad (9)$$

More complex is the situation with  $g_{\omega\rho\pi}$  coupling constant. Assuming vector meson dominance,  $\omega\rho\pi$  vertex appears in a number of processes. For example,  $V \rightarrow \pi^0\gamma$  decay proceeds via



and therefore  $g_{V\pi\gamma} = \frac{g_{VV_1\pi}}{g_{V_1}}$ . So  $g_{VV_1\pi}$  can be determined from  $\Gamma(V \rightarrow \pi^0\gamma)$  and  $\Gamma(V_1 \rightarrow e^+e^-)$ . On the other hand,  $\pi^0 \rightarrow 2\gamma$  decay, in the framework of the vector meson dominance, goes through



and therefore

$$\Gamma(\pi^0 \rightarrow 2\gamma) = \pi\alpha^2 m_\pi^3 \left( \frac{g_{\omega\rho\pi}}{g_\rho g_\omega} \right)^2 .$$

So  $g_{\omega\rho\pi}$  can be extracted from  $\Gamma(\pi^0 \rightarrow 2\gamma)$ ,  $\Gamma(\rho \rightarrow e^+e^-)$ , and  $\Gamma(\omega \rightarrow e^+e^-)$ .

All these methods for  $g_{\omega\rho\pi}$  determination give consistent values:

$$\begin{aligned} (11.7 \pm 0.5)\text{GeV}^{-1} & \text{ from } \Gamma(\rho \rightarrow e^+e^-) \text{ and } \Gamma(\omega \rightarrow \pi^0\gamma) , \\ (12.6 \pm 0.7)\text{GeV}^{-1} & \text{ from } \Gamma(\omega \rightarrow e^+e^-) \text{ and } \Gamma(\rho^+ \rightarrow \pi^+\gamma) , \\ (12.5 \pm 0.9)\text{GeV}^{-1} & \text{ from } \Gamma(\pi^0 \rightarrow 2\gamma), \Gamma(\omega \rightarrow \pi^0\gamma), \Gamma(\rho^+ \rightarrow \pi^+\gamma) , \\ (11.8 \pm 0.5)\text{GeV}^{-1} & \text{ from } \Gamma(\pi^0 \rightarrow 2\gamma), \Gamma(\omega \rightarrow e^+e^-), \Gamma(\rho \rightarrow e^+e^-) . \end{aligned} \quad (10)$$

But if the value of  $g_{\omega\rho\pi}$  is extracted from the experimental  $\omega \rightarrow 3\pi$  decay width, assuming that this decay proceeds through  $\omega \rightarrow \rho\pi$  intermediate state and that the  $g_{\rho\pi\pi}$  coupling constant is determined from the  $\Gamma(\rho \rightarrow 2\pi)$ , one obtains

$$g_{\omega\rho\pi} = (14.3 \pm 0.2) \text{ GeV}^{-1} . \quad (11)$$

This is closer to the chiral model prediction [18]

$$g_{\omega\rho\pi} = \frac{3g_{\rho\pi\pi}^2}{8\pi^2 f_\pi} \approx 14.9 \text{ GeV}^{-1} , \quad f_\pi \approx 93\text{MeV} .$$

$g_{\omega\rho\pi}$  can be estimated also from QCD sum rules [19, 20] with the result  $g_{\omega\rho\pi} = (16 \pm 2)\text{GeV}^{-1}$  [20].

In Monte-Carlo simulation, we have used (11) and  $g_{\phi\rho\pi} \approx -0.81\text{GeV}^{-1}$ , which follows from  $\Gamma(\phi \rightarrow 3\pi)$ . These values assume only  $\rho$ -pole decay mechanism for  $\omega \rightarrow 3\pi$  transition, without a possible  $\omega \rightarrow 3\pi$  contact term [21]. In fact, the uncertainty in these coupling constants does not effect significantly the Monte-Carlo estimates for the detection efficiencies.

## 2.4 $\phi$ - $\rho$ - $\omega$ mixing contribution

$\phi \rightarrow \omega\pi$  vertex is forbidden by  $G$ -parity, which is negative for all three particles. Another way to see this is to notice that it is impossible to construct isospin invariant trilinear coupling between  $\phi$  and  $\omega$  isosinglets and isovector pion.

But the isospin symmetry breaks due to electromagnetic effects and mass difference between u and d quarks. As a result, pure isospin eigenstates  $\omega_I$  and  $\rho_I$  mix and cease to be mass eigenstates. Instead we will have a nondiagonal mass matrix

$$\begin{pmatrix} \rho_I & \omega_I \end{pmatrix} \begin{pmatrix} z_\rho^0 & z_{\omega\rho} \\ z_{\omega\rho} & z_\omega^0 \end{pmatrix} \begin{pmatrix} \rho_I \\ \omega_I \end{pmatrix} .$$

Mass eigenstates (physical  $\rho$  and  $\omega$  mesons) are mixtures of isospin eigenstates, which for small  $\rho$ - $\omega$  mixing angle  $\epsilon_{\omega\rho}$  ( $\sin \epsilon_{\omega\rho} \approx \epsilon_{\omega\rho}$ ) look like

$$\begin{aligned} \rho &= \rho_I - \epsilon_{\omega\rho}\omega_I \\ \omega &= \omega_I + \epsilon_{\omega\rho}\rho_I \end{aligned} .$$

The mixing angle  $\epsilon_{\omega\rho}$  is determined from the condition

$$\begin{pmatrix} \rho_I & \omega_I \end{pmatrix} \begin{pmatrix} z_\rho^0 & z_{\omega\rho} \\ z_{\omega\rho} & z_\omega^0 \end{pmatrix} \begin{pmatrix} \rho_I \\ \omega_I \end{pmatrix} = \begin{pmatrix} \rho & \omega \end{pmatrix} \begin{pmatrix} z_\rho & 0 \\ 0 & z_\omega \end{pmatrix} \begin{pmatrix} \rho \\ \omega \end{pmatrix} ,$$

which gives in the first order in  $z_{\omega\rho}$  and  $\epsilon_{\omega\rho}$  [22] :

$$z_\rho \approx z_\rho^0, \quad z_\omega \approx z_\omega^0, \quad \epsilon_{\omega\rho} = \frac{z_{\omega\rho}}{z_\omega - z_\rho} .$$

Here [22]  $z_V = (M_V - i\frac{\Gamma_V}{2})^2 \approx M_V^2 - iM_V\Gamma_V$  is the resonance complex mass square. So

$$\epsilon_{\omega\rho} = \frac{z_{\omega\rho}}{M_\omega^2 - M_\rho^2 - i(M_\omega\Gamma_\omega - M_\rho\Gamma_\rho)} . \quad (12)$$

As for  $\rho$ - $\omega$  mixing amplitude  $z_{\omega\rho}$ , we will take the value

$$z_{\omega\rho} = (-3800 \pm 370)\text{MeV}^2, \quad (13)$$



which follows from the pion form factor studies [22].

Since  $\rho_I = \rho + \epsilon_{\omega\rho}\omega$ , the presence of the  $\phi \rightarrow \rho_I\pi$  vertex will induce an effective  $\phi \rightarrow \omega\pi$  vertex with a coupling constant  $g_{\phi\omega\pi}^{(\omega\rho)} \approx \epsilon_{\omega\rho}g_{\phi\rho\pi}$ .

The described above picture of  $\rho$ - $\omega$  mixing can be trivially generalized to include mixings with the  $\phi$  meson also [23]:

$$\begin{aligned}\rho &= \rho_I - \epsilon_{\omega\rho}\omega_I - \epsilon_{\phi\rho}\phi_I \\ \omega &= \omega_I + \epsilon_{\omega\rho}\rho_I - \epsilon_{\omega\phi}\phi_I \quad . \\ \phi &= \phi_I + \epsilon_{\phi\rho}\rho_I + \epsilon_{\omega\phi}\omega_I\end{aligned}$$

Due to  $\phi$ - $\rho$  mixing another contribution to the  $\phi \rightarrow \omega\pi$  transition will arise  $g_{\phi\omega\pi}^{(\phi\rho)} \approx \epsilon_{\phi\rho}g_{\omega\rho\pi}$ . Because  $|g_{\omega\rho\pi}| \gg |g_{\phi\rho\pi}|$ , this latter contribution turns out to be of the same order as  $g_{\phi\omega\pi}^{(\omega\rho)}$ . So for the  $g_{\phi\omega\pi}$  coupling constant we will use

$$g_{\phi\omega\pi} = g_{\phi\omega\pi}^{(\omega\rho)} + g_{\phi\omega\pi}^{(\phi\rho)} = \epsilon_{\omega\rho}g_{\phi\rho\pi} + \epsilon_{\phi\rho}g_{\omega\rho\pi} \quad (14)$$

The corresponding contribution in  $e^+e^- \rightarrow \pi^0\pi^0\gamma$  is then determined by equation (7).

The  $\phi$ - $\rho$  mixing parameter  $\epsilon_{\phi\rho}$  can be extracted from the  $e^+e^- \rightarrow \pi^+\pi^-$  experimental data near the  $\phi$ -meson [23]:

$$\epsilon_{\phi\rho} = Z \left( \frac{M_\rho^2 g_\phi}{M_\phi^2 g_\rho} \right) \frac{M_\phi \Gamma_\phi}{M_\phi^2 - M_\rho^2 + iM_\phi \Gamma_\rho(M_\phi^2)}, \quad (15)$$

where  $Z$  is experimentally measured interference magnitude [1]. Taking average values  $Re(Z) = (8 \pm 2) \cdot 10^{-2}$ ,  $Im(Z) = -(3.5 \pm 1.3) \cdot 10^{-2}$  from [1], we obtain

$$\epsilon_{\phi\rho} = (0.72 \pm 0.18) \cdot 10^{-3} - i(0.87 \pm 0.32) \cdot 10^{-3}. \quad (16)$$

## 2.5 $\rho'$ meson contribution

No definite theoretical predictions exist for  $\rho'(1465)$  meson contribution, nor it is definitely known whether the only one radial excitation gives significant contribution in this energy region. We will use the following parameterization for this part of the  $g(x)$  function

$$\begin{aligned}g^{(\rho',\omega)}(x) &= Re^{i\xi} k_\rho \frac{s}{s - M_{\rho'}^2 + iM_{\rho'}\Gamma_{\rho'}} \frac{1}{1 - x + \gamma_\omega} \\ \gamma_\omega &= \frac{1}{s}(m^2 - M_\omega^2 + iM_\omega\Gamma_\omega),\end{aligned} \quad (17)$$

where  $k_\rho = \pi\alpha M_\rho^2 \frac{g_{\rho\omega\pi}g_{\omega\pi\gamma}}{g_\rho}$  corresponds to the  $\rho$ -meson contribution.  $R$  and  $\xi$  parameters were determined by fitting  $\sigma(e^+e^- \rightarrow \omega\pi) = \frac{\sigma(ee \rightarrow \omega\pi \rightarrow \pi^0\pi^0\gamma)}{Br(\omega \rightarrow \pi^0\gamma)}$  cross section to higher energy experimental data from [1]. The fit gives the following values:

$$R = 0.72 \pm 0.03, \quad \xi = 3.25 \pm 0.08. \quad (18)$$

Our results of this fit confirms the conclusions of [25] that the  $\rho'(1465)$  meson contribution is sufficient to describe the existing experimental data in the  $1.05 \div 1.6$  GeV energy range.

Note that we use the PDG [24] values  $M_{\rho'} = 1.465$  GeV and  $\Gamma_{\rho'} = 0.31$  GeV. To simulate roughly a threshold effect due to the dominant  $\rho\pi\pi$  decay of the  $\rho'$  meson, we have assumed, as in [26], that the  $\rho'$ -meson width rises linearly from  $\sqrt{s} = 0.8$  GeV up to  $\sqrt{s} = M_{\rho'}$ , remaining constant above.

## 2.6 Theoretical prediction

Using the estimates for various coupling constants given above, the total cross section can be evaluated for  $e^+e^- \rightarrow \pi^0\pi^0\gamma$  reaction. The result is shown on Fig.1. Note the significant interference effect near  $\phi$  meson, although the  $\phi$ -meson mediated amplitude itself remains small and corresponds to  $Br(\phi \rightarrow \rho\pi \rightarrow \pi^0\pi^0\gamma) \approx 10^{-5}$ , in consistence with [27]. The  $\phi$ - $\rho$ - $\omega$  interference contribution into  $\phi \rightarrow \omega\pi$  transition corresponds to  $Br(\phi \rightarrow \omega\pi) \approx 5.7 \cdot 10^{-5}$  in excellent agreement with the recent experimental result [28]  $(4.8_{-1.7}^{+1.9} \pm 0.8) \cdot 10^{-5}$ , although it should be beared in mind that there may exist also other sources for this transition [29]

## 3 Detector and experiment

SND is a general purpose nonmagnetic detector. This new detector combines advantages of its predecessor ND detector [30] and famous Crystal Ball detector [31], that is a good uniformity over the solid angle due to the spherical shape, a good  $e/\pi$  and  $\gamma/K_L$  separation due to multilayer structure of the electromagnetic calorimeter, and high hermeticity. The main part of the SND detector (Fig.2) is a 3-layer, spherical, highly granulated, NaI(Tl) electromagnetic calorimeter [32]. Tracking system, located in the detector center, consists of two coaxial cylindrical drift chambers. In the radial gap between them a 5 mm thick plastic scintillation counter with a

wavelength shifter fiber readout is placed. From outside the calorimeter is covered by a thick (12 cm) iron absorber, which attenuates remnants of electromagnetic showers. An outer muon/veto system is located outside the absorber. It consists of sheets of plastic scintillator and streamer tubes.

The detailed description of the SND detector can be found elsewhere [7, 8, 9]. Here we repeat only the main points, relevant to this study.

### 3.1 Calorimeter

Each layer of the calorimeter includes 520–560 crystals of eight different shapes. Most of the crystals have shapes of truncated tetrahedral pyramids. The total solid angle covered by the calorimeter is equal to 0.9 of  $4\pi$ . The remaining space is occupied by magnetic structure elements of the storage ring, mainly by quadrupole lenses. Pairs of counters of the first two layers with thickness of  $3X_0$  and  $5X_0$  respectively are sealed together in common containers made of thin (0.1 mm) aluminum foil. In order to improve light collection efficiency and to separate one crystal from another, each crystal is wrapped in aluminized mylar. The gaps between adjacent crystals do not exceed 0.5 mm. The r.m.s. value of the nonuniformity of the light collection efficiency along the crystals is less than 3 %. All the containers are fastened to 5 mm aluminum supporting hemispheres. The outer layer of  $6X_0$  thick counters has a similar design. Thus the total thickness of the calorimeter is  $13.5X_0$  (35 cm) of NaI(Tl).

As photosensitive devices for the calorimeter counters vacuum phototriodes are used [33]. The quantum efficiency of their photocathodes is about 15 %, average gain is 10, and light collection efficiency for individual counters is about 10 %. Signals from phototriodes are amplified by charge sensitive preamplifiers located directly on the counters. Output signals are carried to shaping amplifiers via 20 m long twisted cables. For the trigger needs the calorimeter crystals are logically organized into “towers”. A tower consists of counters located within the same  $18^\circ$  interval in polar and azimuthal directions in all three layers. The number of counters in a tower is 12 at large angles and 6 in the regions close to the beam. In addition to signals from individual counters each tower produces an analog total energy deposition signal and two trigger signals. In order to equalize contributions from different counters into the total energy deposition signal and to obtain equal energy thresholds for trigger signals over the whole calorimeter, all shaping amplifiers are equipped with computer controlled

attenuators, allowing to adjust channels gain in steps of 1/255. The resulting electronics noise is close to 0.3 MeV (r.m.s.). The dependence of the calorimeter energy resolution on photon energies was fitted as [34]

$$\sigma_E/E(\%) = \frac{4.2\%}{\sqrt[4]{E(\text{GeV})}}. \quad (19)$$

The calorimeter energy resolution is determined mostly by the amount of passive material inside the calorimeter. Noticeable contribution comes also from the shower energy leakage due to limited thickness of NaI(Tl) and gaps between crystals. It turned out that the nonuniformity of the light collection efficiency in the NaI(Tl) crystals of the inner calorimeter layer contributes significantly into energy resolution. The simulation of calorimeter response agrees reasonably well with experiment after these effects are included into simulation program.

Absolute energy calibration of the calorimeter is performed by using cosmic muons [35] and Bhabha scattering [34]. The latter process, together with the two-photon annihilation reaction, was also used for the luminosity measurements. The systematic error in the integrated luminosity determination is about 3%.

After the calorimeter calibration with  $e^+e^- \rightarrow e^+e^-$  events, the photon energies turned out to be biased by about 1%. In order to compensate for this bias, the calibration coefficients for photons were corrected accordingly.

### 3.2 Tracking system

The tracking system consists of two cylindrical drift chambers. The length of the chamber closest to the beam is 40 cm, its inner and outer diameters are 4 and 12 cm respectively. The corresponding dimensions of the outer chamber are 25, 14 and 24 cm. Both chambers are divided into 20 jet-type cells in azimuthal plane. Each cell contains 5 sense wires. The longitudinal coordinate is measured by the charge division method with an accuracy of 3 mm. In addition, a cathode strip readout for inner and outer layers provides the improvement of the latter value to 0.5 mm. The outer drift chamber improves pattern recognition for multiparticle events. The overall angular resolution of the drift chamber system is 0.5 and 1.7 degrees in azimuthal and polar directions respectively. The impact parameter resolution is 0.5 mm. The solid angle coverage for the inner chamber is 96 % of  $4\pi$ .

### 3.3 Muon detector

The SND muon system consists of plastic scintillation counters and streamer tubes [36]. It is intended mainly for cosmic background suppression for the events without charged particles. The probability of its triggering by the events of the reaction  $e^+e^- \rightarrow \gamma\gamma$  at the maximum available energy is less than 1 %. Muons of the process  $e^+e^- \rightarrow \mu^+\mu^-$ , starting from the beam energy about 500 MeV, penetrate through the absorber and hit the muon detector.

### 3.4 Trigger

The three-level trigger of the detector selects events of different types: events with photons only, events with charged particles, and cosmic muon events for the detector calibration. The drift chamber first level trigger (FLT) searches for tracks in the drift chambers with impact parameter  $\Delta r < 20$  mm. The calorimeter FLT uses the total energy deposition in the calorimeter and double coincidences of calorimeter towers with a threshold of 30 MeV.

Detector electronics provides also signals for a second level trigger. But at present the second level trigger proved to be unnecessary and was not implemented, although a slot is left for it in the electronics.

The third level trigger (TLT) is implemented as a special fast computer code on a main data acquisition computer. It checks events before recording them on tape, rejects cosmic events with charged trigger, and suppresses beam-related background using  $z$ -coordinates of tracks, measured by drift chambers. In addition TLT identifies collinear events of Bhabha scattering and  $2\gamma$  annihilation. These events are used for monitoring the collider luminosity.

### 3.5 Data acquisition system

SND data acquisition system is based on the fast electronics modules KLUKVA [37], developed in BINP specially for purpose of the detectors CMD-2, KEDR and SND.

Analog signals from the detector come to the front-end amplifiers and shapers, located near the detector. Then the signals are transmitted via screened twisted pair cables to the digitizing modules (ADC, TDC, etc) in KLUKVA crates. Logical signals from discriminators in KLUKVA crates

are collected by the first level trigger interface modules. After 1  $\mu s$ , needed for FLT decision, FLT generates a signal to start digitizing. The contents of KLUKVA digitizing modules are read into the RAMs of Output Processor modules (OP), located in KLUKVA crates. This procedure finishes in 120  $\mu s$ . There are two independent RAMs for events in each OP and one event can be stored in digitizing modules, such a fast buffering greatly decreases dead time. The total dead time in KLUKVA is 200  $\mu s$  per event selected by FLT. The data from OP RAMs are read by the VAX server 3300 through the CAMAC interface modules with the rate of 2 ms/event. The TLT program can process events with a maximum rate of 45Hz. Finally the processed events are put on 8 mm 5 GB EXABYTE tapes.

### 3.6 Experiment PHI96

A description of the PHI96 experiment was published in [11]. The PHI96 experiment was carried out from February 1996 up to January 1997. Seven successive scans were performed in 14 energy points in the range  $2E$  from 980 to 1044 MeV.

The data sample, which was analyzed, corresponds to an integrated luminosity of  $4.5 pb^{-1}$ , collected by SND in the narrow energy interval near the  $\phi$ -meson. Estimated number of produced  $\phi$ -mesons equals to  $8.3 \cdot 10^6$ .

## 4 Event selection

While studying the channel

$$e^+e^- \rightarrow \omega\pi^0 \rightarrow \pi^0\pi^0\gamma \quad (20)$$

one should be aware about the possible background from the following processes

$$e^+e^- \rightarrow \phi \rightarrow \eta\gamma \rightarrow 3\pi^0\gamma, \quad (21)$$

$$e^+e^- \rightarrow \phi \rightarrow K_S K_L \rightarrow \text{neutral particles}. \quad (22)$$

A primary selection of the  $e^+e^- \rightarrow \omega\pi^0 \rightarrow \pi^0\pi^0\gamma$  candidates was done according to following criteria:

- the event must contain exactly 5 photons in the calorimeter and have no charged particles,
- the azimuthal angle of any final photon lies within the interval  $27^\circ < \theta < 153^\circ$ ,

- the total (normalized over  $2E$ ) energy deposition of final photons is in the range  $0.8 \leq E_{tot}/2E \leq 1.1$ ,
- the normalized full momentum of the event ( $P_{tot}/2E$ ) is less than 0.15.

The two latter conditions eliminate the main part of the background, originated from the  $\phi \rightarrow K_L K_S$  decay, but they do not help much against another background, coming from the process (21).

It is interesting to check whether we really have two  $\pi^0$ -s in our 5-photon events. It is unlikely for the most energetic photon to come from  $\pi^0$  decay in either (20), (21) or  $e^+e^- \rightarrow K_L K_S \rightarrow 2\pi^0 K_L$  reactions. It is also not likely for  $\pi^0$  to produce the two softest photons. If we discard the corresponding combinations, only two possibilities (2,4),(3,5) and (2,5),(3,4) are left for the photons to compose  $\pi^0$ 's (photons are arranged according to their energy, the most energetic being the first one). A combined 2-dimensional plot of invariant masses of these photon pairs ( $M_{24}$  versus  $M_{35}$  plus  $M_{25}$  versus  $M_{34}$ ) is shown in Fig.3. We clearly see that our 5-photon events are predominantly  $2\pi^0$  events also. Besides, Fig.3 illustrates that background (21) produces a wider distribution. This can be used for the rejection of this background. For this purpose, a kinematic fit was performed for each 5-photon event under the assumption that there are two  $\pi^0$ 's in the final state and energy-momentum balance holds within the experimental accuracy. A  $\chi^2$  of this fit ( $\chi_{\pi^0\pi^0\gamma}^2$ ) can be used for the background rejection.

Background from (21) simulates  $\pi^0\pi^0\gamma$  events mainly due to loss of photons through the openings in the calorimeter around detector poles and/or merging of close photon pairs. When photons merge in the calorimeter, the corresponding electromagnetic shower is, as a rule, broader in transverse direction than the electromagnetic showers from the single photons. This circumstance can be used to discriminate against merged photons and so against a great deal of background (21). The corresponding parameter ( $\zeta_\gamma$ ) is described in [38]. A 2-dimensional distributions of our events in the  $\chi_{\pi^0\pi^0\gamma}^2, \zeta_\gamma$  plane, as well as Monte-Carlo simulated (20) signal events and (21) background events (Fig.4), indicate that our signal events are almost completely bound in the  $\zeta_\gamma < 20, \chi_{\pi^0\pi^0\gamma}^2 < 40$  area. This was confirmed by experimental events outside of the  $\phi$ -meson, where there should be no background from the process (21).

On the basis of these considerations, we have chosen the following two sets (Cut I and Cut II) of selection criteria for the channel (20) separation (in addition to the primary selection rules, described above):

- the normalized full momentum of the event is less than 0.1 (for Cut I),
- there are two  $\pi^0$ -mesons in the event, that is, one can find two distinct pairs of photons with invariant masses within  $\pm 30$  MeV from the  $\pi^0$  mass,
- $\chi_{\pi^0\pi^0\gamma}^2$ , the  $\chi^2$  of the kinematic fit, is less than 20 for Cut I, or is less than 40 for looser Cut II,
- $\zeta_\gamma$ , the parameter describing the transverse profile of the electromagnetic shower, is less than 0 for Cut I, or is less than 20 for Cut II.

One more source of background is a recently observed process [12, 39]:

$$e^+e^- \rightarrow \phi \rightarrow f_0\gamma \rightarrow \pi^0\pi^0\gamma . \quad (23)$$

The recoil mass of the photon from this process is peaked at the  $f_0$ -meson mass and this peculiarity can be used to separate a great deal of such events from the events of process (20). We have chosen the  $M_\gamma < 700\text{MeV}$  condition as one more cut to select events from the process (20), where  $M_\gamma$  stands for the photon recoil mass.

After applying these cuts, the  $\omega$ -meson peak is clearly seen in the invariant mass of  $\pi^0$  and  $\gamma$  (for each  $\pi^0\pi^0\gamma$  event, from two possible  $(\pi^0, \gamma)$  combinations, the one is taken, which has  $M_{\pi^0\gamma}$  closest to  $M_\omega$ ), as it is illustrated by Fig.5 (Cut I). Finally, to extract channel (20), the  $750\text{MeV} < M_{\pi^0\gamma} < 820\text{MeV}$  condition was added to the above mentioned cuts.

The  $M_{\pi^0\gamma}$  histograms were fitted by a function

$$p_1 \exp\left(-\frac{(x - p_2)^2}{2p_3^2}\right) + p_4 .$$

The fit indicates a good agreement between the experiment and simulation. For the 2356 MC events, which passed Cut I, the fitted value of the constant term is  $p_4 = 9.2 \pm 1.3$ . Since in the  $750\text{MeV} < M_{\pi^0\gamma} < 820\text{MeV}$  interval we have 35 histogram bins, such background constant corresponds to  $322 \pm 46$  combinatorial background events, that is about 14%. The same conclusion follows also for Cut II.

For the 560 experimental events which passed Cut I, the following background constant was obtained:  $p_4 = 3.3 \pm 0.9$ , which correspond to  $116 \pm 32$  background events. Subtracting the expected combinatorial background of  $76 \pm 11$ , we can estimate the residual background from (21), (22), (23), as



$40 \pm 34$  events ( $\sim 7\%$ ). For Cut II this background was found to be twice higher, that is  $133 \pm 38$  background events from the selected 864 experimental events ( $\sim 15\%$ ).

On the other hand, Monte Carlo studies indicate the following probabilities for events from the main background sources to pass Cut I:  $(2.7 \pm 0.3) \cdot 10^{-4}$  for process (21), and  $(2.9 \pm 0.2) \cdot 10^{-2}$  for process (23). This corresponds to  $28 \pm 3$  background events from process (21) and  $22 \pm 4$  from process (23). So the total number of background events from these sources is estimated to be  $50 \pm 5$ . For Cut II we expect  $116 \pm 8$  and  $27 \pm 5$  background events, respectively, or in total  $143 \pm 10$  events. These numbers are in a good agreement with those obtained from the above mentioned fitting of the  $\omega$ -meson peak.

To check the accuracy of Monte Carlo simulation the following procedure was applied. For the above described Cut I and Cut II, one of the parameters is released and the resulting experimental distribution  $H_{EXP}$  for this parameter is compared with the sum of MC predictions for the signal  $H_{\omega\pi^0}$  and expected backgrounds from (21) and (23) sources:  $H_{MC} = k_{\omega\pi^0}H_{\omega\pi^0} + k_{\eta\gamma}H_{\eta\gamma} + k_{f^0\gamma}H_{f^0\gamma}$ . The normalization coefficients  $k_{\eta\gamma}$  and  $k_{f^0\gamma}$  are determined by the total statistics of generated MC samples for this reactions. The normalization coefficient for the signal  $k_{\omega\pi^0}$  is then determined from the condition that  $H_{EXP}$  and  $H_{MC}$  histograms have the equal total numbers of events. Note that any variation in the  $k_{\omega\pi^0}$  coefficient indicates some systematics and/or other background sources, not accounted for in the comparison. For Cut I the averaged deviation turned out to be 3% and for Cut II – 4%.

The distributions for all parameters used in event selections show good agreement between *MC* and experiment. This indirectly indicates that the possible background from process (22) is rather small and does not exceed  $\sim 5\%$ . As an example, on Fig.6 we present  $M_{\pi^0\gamma}$  distributions.

## 5 Data analysis and results

We assume the following parameterization for the visible (detection) cross section  $\sigma_v$ :

$$\sigma_v = \epsilon[1 + \delta(s)]\sigma(s) + kb\sigma_B(s) , \quad (24)$$

where  $\epsilon$  is the detection efficiency for the process (20),  $\delta(s)$  accounts for the radiative corrections, which are calculated according to the standard

procedure [40],  $\sigma_B(s)$  is a background cross section, which was assumed to coincide with  $\sigma(e^+e^- \rightarrow \eta\gamma \rightarrow 3\pi^0\gamma)$ ,  $k$  is the background suppression factor,  $b$  is described below. Finally,  $\sigma(s)$  is a cross section of the process under investigation. Because we are interested in  $\sigma(s)$  in a narrow energy interval, we have taken

$$\sigma(s) = [\sigma_0 + \sigma'(2E - M_\phi)] |R|^2, \quad R = 1 - Z \frac{m_\phi \Gamma_\phi}{s - M_\phi^2 + iM_\phi \Gamma_\phi}. \quad (25)$$

The detection efficiency  $\epsilon$  was calculated using Monte-Carlo simulation in conditions of individual scans for various energies. Detection efficiencies do not show any significant energy dependence. So we have taken an efficiency value averaged over scans and energies,  $\epsilon = (29.7 \pm 0.25)\%$  (only statistical error is indicated) as a fair estimate for Cut II.

For a tighter Cut I some systematic errors could be expected. To estimate this systematics, we compared the numbers of rejected events for each parameter of Cut I in the above described  $H_{EXP}$  and  $H_{MC}$  distributions. The following correction factors ( $\epsilon_{MC}/\epsilon_{EXP}$ ) were obtained:  $1.032 \pm 0.018$  for  $P_{tot}/2E$ ,  $1.015 \pm 0.023$  for  $\chi_{\pi^0\pi^0\gamma}^2$ ,  $1.074 \pm 0.028$  for  $\zeta_\gamma$ ,  $1.015 \pm 0.023$  for  $M_\gamma$  and  $0.98 \pm 0.028$  for  $M_{\pi^0\gamma}$ . In total, the Monte Carlo simulation overestimates the detection efficiency  $1.12 \pm 0.06$  times, if we assume that there are no correlations between the used selection parameters. With this correction factor taken into account, an average detection efficiency  $\epsilon = (20.7 \pm 1.1)\%$  was obtained for Cut I.

The background suppression factor  $k$  was also assumed to be energy independent. It was calculated using  $\sim 2.15 \cdot 10^5$  simulated events from the process (21) and equals  $(2.7 \pm 0.3) \cdot 10^{-4}$  for Cut I and  $(1.10 \pm 0.06) \cdot 10^{-3}$  for Cut II.

As we have seen above, for Cut I a relatively large fraction of background is expected from process (23). Some small amount of  $\phi \rightarrow K_S K_L$  decay related background (22) is also not excluded. To take into account these and other  $\phi$ -meson related backgrounds, the factor  $b$  is introduced in (24). It is assumed that the different energy dependencies of various background cross-sections is not relevant at the present level of statistical accuracy and so they all can be approximated by the  $\sigma(e^+e^- \rightarrow \eta\gamma)$  behavior.

The fit results are given in the Table 1.

Because of specific behavior of the interference effect, it can happen that the resonant background cancels the interference dip and so mimics the no-interference no-background situation, making it impossible to distinguish

parameter	Cut I	Cut II
$\sigma_0$ (nb)	$0.61 \pm 0.06$	$0.63 \pm 0.05$
$\sigma'$ (nb/MeV)	$(0.43 \pm 0.24) \cdot 10^{-2}$	$(0.49 \pm 0.21) \cdot 10^{-2}$
$\text{Re}(Z)$	$0.1 \pm 0.1$	$0.12 \pm 0.08$
$\text{Im}(Z)$	$-0.19 \pm 0.15$	$0.05 \pm 0.08$
$b$	$2.8 \pm 1.9$	$0.1 \pm 0.3$
$\chi^2/d.f.$	11.0/10	14.5/10

Table 1: Fitted parameters for the fit with the interference.

between these two options during the fit. This is confirmed by the following observation: If we assume no interference effects in the  $\sigma(s)$  and just take  $\sigma(s) = \sigma_0 + \sigma'(2E - M_\phi)$ , this linear fit will result in the Table 2.

parameter	Cut I	Cut II
$\sigma_0$ (nb)	$0.58 \pm 0.05$	$0.64 \pm 0.03$
$\sigma'$ (nb/MeV)	$(0.44 \pm 0.23) \cdot 10^{-2}$	$(0.58 \pm 0.20) \cdot 10^{-2}$
$b$	$0.2 \pm 1.1$	$0.2 \pm 0.2$
$\chi^2/d.f.$	12.1/12	16.7/12

Table 2: Fitted parameters for the linear fit.

In spite of our considerations above, from which one could expect  $b \approx 1$  for Cut II (and  $b \approx 2$  for Cut I – the expected background is indeed dominated by the process (21) for Cut II, while for Cut I half of the background originates due to process (23)), this fit indicates no-background for Cut II, so in fact providing an indirect evidence in favour of the interference effect!

As we see, the results for Cut I and Cut II are consistent after the detection efficiency for Cut I is corrected against estimated systematics. Of course, we do not know if there is some part of systematic errors left uncorrected for Cut I. On the other hand, for Cut II more background is expected and we can neither very precisely estimate this background (for example, the part coming from (22)) nor subtract it during fit (note that all of the above fits gave very large errors for the background constant  $b$ ).

Therefore we select as a fair estimates for the  $\sigma_0$  and  $\sigma'$  parameters the mean values between Cut I and Cut II, and as systematic errors we take the difference between them. Another part ( $\sim 3\%$ ) of the systematic error can arise from the luminosity measurement.

One more source of systematics is a possibility that a sixth false photon is piled up on the five photon event due to the beam related background. This effect is hard to simulate, so the MC efficiency is expected to be

somewhat overestimated. To find the correction factor, the 6-photon events were investigated as described in the next section. This factor turned out to be  $1.04 \pm 0.02$ . Our final results in this analysis, which include this correction factor, as well as the estimated total systematic error, are

$$\begin{aligned}\sigma_0 &= (0.64 \pm 0.08) \text{ nb} \\ \sigma' &= (0.48 \pm 0.27) \cdot 10^{-2} \text{ nb/MeV}\end{aligned}\tag{26}$$

As for  $Re(Z)$  and  $Im(z)$ , the still high level of background precludes an estimation of these parameters. For Cut I, which is more pure against background,  $Im(Z) = -0.19 \pm 0.15$  is only one sigma effect.

We have also tried  $\sigma(s) = \zeta \sigma_{th}(s)$  in a fit, where  $\sigma_{th}(s)$  is the theoretical prediction (including  $\rho'$ -meson) for the reaction (20), discussed at the beginning. The fitted parameters are given in the Table 3.

parameter	Cut I	Cut II
$\zeta$	$1.19 \pm 0.09$ ( $1.54 \pm 0.12$ )	$1.29 \pm 0.08$ ( $1.68 \pm 0.11$ )
$b$	$2.7 \pm 1.0$ ( $2.8 \pm 1.0$ )	$1.1 \pm 0.3$ ( $1.2 \pm 0.3$ )
$\chi^2/d.f.$	11.7/13 (11.7/13)	17.5/13 (17.4/13)

Table 3: Fitted parameters for the fit with the theoretical cross-section. The parameters for the fit without  $\rho'$  meson are also given in the parenthesis. The indicated  $\zeta$ -values should be multiplied by the correction factor  $1.04 \pm 0.02$ , as discussed in the text.

The obtained cross section is close enough to the theoretical prediction, when  $\rho'$ -meson contribution is also included, although the experimental cross section is somewhat ( $\sim 25\%$ ) higher. This can indicate that more than one radial excitation of the  $\rho$ -meson contributes or that the used higher energy  $ee \rightarrow \omega\pi$  cross section is subject to some systematics, which we do not take into account while extracting the  $\rho'$  related parameters  $R$  and  $\xi$ . Finally, our parameterization for the  $\rho'$  contribution can also be not quite adequate (for example, we had only roughly modeled the energy dependence of the  $\rho'$  width). In any case, the experimental cross section can not be explained by only the  $\rho$ -meson tail, which gives about 1.6 times lower result.

## 6 Observation of the interference effect

During the study of the reaction  $e^+e^- \rightarrow \omega\pi^0 \rightarrow \pi^+\pi^-\pi^0\pi^0$ , the  $\phi \rightarrow \omega\pi^0$  decay was observed for the first time with the branching ratio about  $5 \cdot 10^{-5}$

[28]. The decay reveals itself as an interference wave on the nonresonant cross section of the process  $e^+e^- \rightarrow \omega\pi^0$ . In principle, a similar picture should be observed in neutral channel (20), as was explained above in the theoretical introduction. Really the whole situation here looks more complicated because of other  $\phi$  meson neutral decays like  $\phi \rightarrow \rho^0\pi^0$ ,  $\phi \rightarrow f_0\gamma$ ,  $\sigma\gamma$  [39], which have the same final state and interfere with the process (20). The interference amplitude with the  $\phi \rightarrow \rho^0\pi^0$  decay is expected to be about 10%, which is close to the value 17% due to  $\phi \rightarrow \omega\pi^0$  decay, obtained in [28]. In our preceding study [12] of the reaction (20), we did not observe the interference because of small statistics and nonresonant background.

In the present work the analysis given above also does not reveal the interference effect with certainty in spite of higher statistics, because the background is still high. Here we present another analysis specially dedicated to the interference observation.

The events selected by the criteria, described above, were divided into following 3 classes:

- 1)  $\chi_{\pi^0\pi^0\gamma}^2 < 20$ ,  $|M_{\pi^0\gamma} - 782| < 30$ ,  $\zeta_\gamma < -5$ ;
- 2)  $\chi_{\pi^0\pi^0\gamma}^2 < 20$ ,  $30 < |M_{\pi^0\gamma} - 782| < 60$ ,  $\zeta_\gamma < -5$ ;
- 3)  $\chi_{\pi^0\pi^0\gamma}^2 < 20$ ,  $|M_{\pi^0\gamma} - 782| < 30$ ,  $N_\gamma = 6$ .

The 6-photon events were put into the last class. It was done to investigate a probability that sixth false photon is superimposed on the five photon event due to beam-related background. In the kinematic fit one of photons was supposed to be spare.

The simulation shows that the signal to background ratio is maximal in class 1, which was used later for investigation of the interference effects. The contribution of process (20) in class 2 is about 10 times lower, which allows to extract from the data the resonant background from the above mentioned processes with  $f^0\gamma$ ,  $K_S K_L$  and  $\eta\gamma$  intermediate states. Using the ratio of the resonant background in classes 1 and 2 obtained from the simulation, one can estimate the background in class 1, when the resonant background in class 2 is determined from the experimental data. The ratio of the background event numbers in the regions  $|M_{\pi^0\gamma} - 782| < 30$  and  $30 < |M_{\pi^0\gamma} - 782| < 60$  weakly depends on the limits on  $\chi_{\pi^0\pi^0\gamma}^2$  and  $\zeta_\gamma$  parameters. For the process (23) this ratio varies in the limits  $1.09 \div 1.12$ , while for the process (21) — from 0.9 to 1.07. These variations are within the statistical accuracy of the corresponding MC simulation. The value

$1.1 \pm 0.2$  was taken for this ratio.

The visible cross section in each class was presented in the following form:

$$\sigma_{vis} = \alpha_i \epsilon [1 + \delta(s)] \sigma(s) + \beta_i \sigma_B(s)$$

where  $\sigma(s)$  is given by (25),  $\epsilon$  is the total over all classes detection efficiency for the  $e^+e^- \rightarrow \omega\pi^0 \rightarrow \pi^0\pi^0\gamma$  process, and  $\delta(s)$  represents the standard radiative corrections [40]. As above,  $\sigma_B(s)$  is assumed to coincide with  $\sigma(e^+e^- \rightarrow \eta\gamma \rightarrow 3\pi^0\gamma)$ . The parameters  $\alpha_i$  are the probabilities for our process to be found in  $i$ -th class, the parameters  $\beta_i$  represent nonresonant cross section in  $i$ -th class, normalized to the  $e^+e^- \rightarrow \phi \rightarrow \eta\gamma$  process cross section. As it was already mentioned, the  $\phi$  meson excitation curve was described by the main background process (21). The differences in excitation curves for different background processes were neglected at the present level of accuracy. The fitting of the visible cross section was done for all three classes simultaneously. The parameters  $\sigma_0$ ,  $\sigma'$ ,  $Re(Z)$ ,  $Im(Z)$ ,  $\alpha_i$ ,  $\beta_i$  except  $\beta_1$  and  $\alpha_1$  were free.  $\beta_1$  were found from the expression  $\beta_1 = (1.1 \pm 0.2) \cdot \beta_2$ ,  $\alpha_1$  – from normalization  $\sum \alpha_i = 1$ . The detection efficiency  $\epsilon=27.5\%$ , obtained from the simulation, does not depend on the energy. The coefficients  $\alpha_i$  are also energy independent. The total number of fit parameters is 8. In each class the cross section was measured in 15 points. The following values of interference parameters were obtained

$$\begin{aligned} Re(Z) &= 0.036 \pm 0.052, \\ Im(Z) &= -0.186 \pm 0.063. \end{aligned} \tag{27}$$

The statistical errors for this parameters are much higher than the systematical ones. The quoted errors include the systematics due to background subtraction in class 1.

The ratio  $\alpha_3/(\alpha_1 + \alpha_3)$  gives the probability that the signal event will be lost because the additional background photon is superimposed on it. This probability turned out to be  $0.04 \pm 0.02$  and the corresponding correction factor was included in the  $\sigma_0$  and  $\sigma'$  determination in the previous section.

The detected cross section for class 1 and the fitted curve with  $\chi^2/d.f. = 11.9/11$  are shown in Fig.7. The fitted resonant background is also shown at the bottom. One could see, that in spite of imposed strong cuts in class 1, the resonant background is about one third of interference amplitude wave and is the dominant source of systematic error in  $Z$ . This systematic error is estimated to be about 6%.

## 7 Conclusions.

In conclusion, we obtained in the present work the following values of the  $e^+e^- \rightarrow \omega\pi^0 \rightarrow \pi^0\pi^0\gamma$  process cross section parameters:

$$\begin{aligned}\sigma_0 &= (0.64 \pm 0.08) \text{ nb}, \\ \sigma' &= (0.0048 \pm 0.0027) \text{ nb}/MeV, \\ Re(Z) &= 0.036 \pm 0.052, \\ Im(Z) &= -0.186 \pm 0.063.\end{aligned}\tag{28}$$

The measured interference amplitude is three standard deviation above zero. The measured in [28] interference amplitude for the decay  $\phi \rightarrow \omega\pi^0$  is  $Re(Z) = 0.104 \pm 0.029$ ,  $Im(Z) = -0.118 \pm 0.031$ . Our calculation of the interference amplitude for the decay  $\phi \rightarrow \rho\pi^0 \rightarrow \pi^0\pi^0\gamma$ , in the framework of the model described in the theoretical introduction, gives  $Re(Z) = -0.079$ ,  $Im(Z) = -0.053$ . The sum of these contributions  $Re(Z) = 0.025$ ,  $Im(Z) = -0.171$  agrees with our measurement. Otherwise stated, if one subtract from the interference amplitude, measured in this work, the expected contribution from the  $\phi \rightarrow \rho\pi^0$  transition given above, the  $\phi \rightarrow \omega\pi$  decay branching ratio can be estimated to be  $5.4 \cdot 10^{-5}$  with almost 100% errors, which should be compared to  $(4.8_{-1.7}^{+1.9} \pm 0.8) \cdot 10^{-5}$  from [28]. Note that we did not make a theoretical estimate for contribution into interference amplitude from the processes  $\phi \rightarrow f_0\gamma$ ,  $\sigma\gamma \rightarrow \pi^0\pi^0\gamma$ . More experimental information about these transitions is required to estimate such contribution correctly.

The measured nonresonant cross section at  $\phi$ -meson  $\sigma(e^+e^- \rightarrow \omega\pi^0) = \sigma(e^+e^- \rightarrow \omega\pi^0 \rightarrow \pi^0\pi^0\gamma)/Br(\omega \rightarrow \pi^0\gamma) = (7.5 \pm 0.9) \text{ nb}$  agrees with the result  $(8.7 \pm 1.0 \pm 0.7) \text{ nb}$  from [1] and with the result  $(8.2 \pm 0.2 \pm 0.9) \text{ nb}$  from [28] in channel with charged pions  $e^+e^- \rightarrow \omega\pi^0 \rightarrow \pi^+\pi^-\pi^0\pi^0$ , as well as with the preliminary CMD-2 result [41]  $(7.2 \pm 0.5) \text{ nb}$ . Such nonresonant cross section can not be explained by only  $\rho$ -meson contribution, which is about 1.6 times lower. Although the inclusion of the  $\rho'(1465)$  meson in the fit improves somewhat the agreement between the theoretical prediction and the experiment, the question about  $\rho$ -meson radial excitations lies beyond the scope of this work, because it requires an experimental information for higher energies.

At last, in Table 4 we provide numerical values of the measured cross section  $\sigma(e^+e^- \rightarrow \omega\pi^0 \rightarrow \pi^0\pi^0\gamma) = \frac{\sigma_v(s)}{\epsilon[1+\delta(s)]}$ .

$\sqrt{s}$ , MeV	cross section, nb
984.1	$0.57 \pm 0.11$
1005.0	$0.56 \pm 0.14$
1010.7	$0.47 \pm 0.10$
1016.2	$0.55 \pm 0.10$
1017.1	$0.48 \pm 0.10$
1018.1	$0.56 \pm 0.08$
1019.1	$0.59 \pm 0.05$
1020.0	$0.51 \pm 0.07$
1021.0	$0.74 \pm 0.11$
1021.9	$0.81 \pm 0.14$
1022.7	$0.55 \pm 0.21$
1028.0	$0.53 \pm 0.12$
1033.7	$0.97 \pm 0.19$
1039.8	$0.96 \pm 0.25$
1060.0	$1.08 \pm 0.31$

Table 4: Measured cross section  $\sigma(e^-e^+ \rightarrow \omega\pi^0 \rightarrow \pi^0\pi^0\gamma)$  (mean values between Cut I and Cut II, corrected by the factor 1.04, as discussed in the text). Only statistical errors are indicated. Systematic errors are estimated to be about 5%.

## 8 Acknowledgement

This work is supported in part by Russian Fund for basic researches, grants No. 99-02-16813 and 96-15-96327.



## References

- [1] S. I. Dolinsky et al., Phys. Rept. **202** (1991) 99.
- [2] S. I. Dolinsky et al., Phys. Lett. **B 174** (1986) 453.
- [3] H. Leutwyler, *in* Proc. Workshop on Chiral Dynamics: Theory and Experiments (Lecture Notes in Physics 452), A. M. Bernstein and B. R. Holstein, editors; Springer, 1995. (hep-ph/9409423).  
Ulf-G. Meißner, Rept. Prog. Phys. **56** (1993), 903. (hep-ph/9302247).
- [4] M. Bando, T. Kugo and K. Yamawaki, Phys. Rept. **164** (1988) 217.  
Ulf-G. Meißner, Phys. Rept. **161** (1988) 213.
- [5] N. Albrecht et al., Phys. Lett. **B 185** (1987) 223.
- [6] S. I. Eidelman and V. N. Ivanchenko, Phys. Lett. **B 257** (1991) 437.  
S. I. Eidelman and V. N. Ivanchenko, Nucl. Phys. Proc. Suppl. **55C** (1997) 181.
- [7] V.M.Aulchenko et al., *in* Proc. Workshop on Physics and Detectors for DAFNE (Frascati, 1991), p. 605.
- [8] S.I. Serednyakov et al., *in* Proc. Instrumentation for colliding beam physics (Novosibirsk, 1990), p. 360.
- [9] V.M.Aulchenko et al., Novosibirsk preprint INP-99-16 (in Russian).
- [10] G. M. Tumaikin, *in* Proc. 10th Intern. Conf. on High Energy Particle Accelerators (Serpuukhov, 1977), vol. 1, p. 443.
- [11] M. N. Achasov et al., Novosibirsk preprint BUDKERINP-96-47.
- [12] M. N. Achasov et al., Novosibirsk preprint BUDKERINP-97-78 (hep-ex/9710017).
- [13] Kay R. Jamison, An unquiet mind, Vintage Books, New York, 1996.
- [14] J.P. Perez-Y-Jorba and F.M. Renard, Phys. Rept. **31C** (1977) 1.
- [15] W. A. Bardeen and W. K. Tung, Phys. Rev. **173** (1968) 1423.
- [16] S. I. Eidelman and E. A. Kuraev, Novosibirsk preprint 85-101 (1985).  
A. B. Arbuzov, O. O. Voskresenskaya and E. A. Kuraev, Dubna preprint JINR-E2-95-430 (1995).

- [17] A. C. Hearn, Reduce user's manual, Rand Publication, 1989.
- [18] O. Kaymakcalan, S. Rajeev and J. Schechter, Phys. Rev. **D 30** (1984) 594.
- [19] M. V. Margvelashvili and M. E. Shaposhnikov, Z. Phys. **C 38** (1988) 467.  
V. M. Braun and I. E. Filyanov, Z. Phys. **C 44** (1989) 157.
- [20] M. Lublinsky, Phys. Rev. **D 55** (1997) 249.
- [21] S. Rudaz, Phys. Lett. **145B** (1984) 281.  
E. A. Kuraev and Z. K. Silagadze, Phys. Atom. Nucl. **58** (1995) 1589.
- [22] H. B. O'Connell, B. C. Pearce, A. W. Thomas and A. G. Williams, Prog. Part. Nucl. Phys. **39** (1997) 201. (hep-ph/9501251).  
H. B. O'Connell, B. C. Pearce, A. W. Thomas and A. G. Williams, Phys. Lett. **B 354** (1995) 14
- [23] A. Bramon, Phys. Rev. **D24** (1981) 1994.
- [24] Review of Particle Physics, Eur. Phys. J. **C3** (1998) 28.
- [25] A. B. Clegg and A. Donnachie, Z. Phys. **C62** (1994) 455.  
A. Donnachie and A. B. Clegg, Phys. Rev. **D51** (1995) 4979.
- [26] J. Buon et al., Phys. Lett. **118B** (1982) 221.
- [27] N. N. Achasov and V. N. Ivanchenko, Nucl. Phys. **B 315** (1989) 465.
- [28] M. N. Achasov et al., Phys. Lett. **B449** (1999) 122 (hep-ex/9901020).  
M. N. Achasov et al., Novosibirsk preprint BUDKERINP-98-65 (hep-ex/9809013).
- [29] N. N. Achasov and A. A. Kozhevnikov, Int. J. Mod. Phys. **A7** (1992) 4825.  
V. A. Karnakov, Sov. J. Nucl. Phys. **42** (1985) 634.
- [30] V. B. Golubev et al., Nucl. Instr. and Meth. **227** (1984) 467.
- [31] E. D. Bloom and C. Peck, Ann. Rev. Nucl. Sci. **33** (1983) 1.  
K. Wachs et al., Z. Phys. **C 42** (1989) 33.
- [32] A. D. Bukin et al., Phys. At. Nucl. **56** (1993) 1494 ( Yad. Fiz. **56** (1993) 75 ).

- [33] P. M. Beschastnov et al., Nucl. Instr. and Meth. **A 342** (1994) 477.  
V. V. Anashin et al., Nucl. Instr. and Meth. **A 379** (1996) 522.
- [34] M. N. Achasov et al., Nucl. Instr. and Meth. **A 411** (1998) 337.
- [35] M. N. Achasov et al., Nucl. Instr. and Meth. **A 379** (1996) 505.
- [36] V. M. Aulchenko et al., Novosibirsk preprint INP 85–122, 1985.
- [37] V. M. Aulchenko et al., Nucl. Instr. and Meth. **A 409** (1998) 639.  
V. M. Aulchenko et al., *in* Proceedings of the International Conference on Calorimetry in High Energy Physics, FNAL, 29 Oct – 1 Nov, 1990.
- [38] M. G. Bekishev and V. N. Ivanchenko, Nucl. Instr. and Meth. **A 361** (1995) 138.  
A. V. Bozhenok, V. N. Ivanchenko and Z. K. Silagadze, Nucl. Instr. and Meth. **A 379** (1996) 507.
- [39] M. N. Achasov et al., hep-ex/9711023.  
V. M. Aulchenko et al., Phys. Lett. **B440** (1998) 442.  
(hep-ex/9807016).
- [40] E. A. Kuraev and V. S. Fadin, Sov. J. Nucl. Phys. **41** (1985) 466.  
O. Nicosini and L. Trentadue, Phys. Lett. **196B** (1987) 551.  
G. Bonneau and F. Martin, Nucl. Phys. **B27** (1971) 381.
- [41] R. R. Akhmetshin et al., Novosibirsk preprint BUDKERINP-99-11.

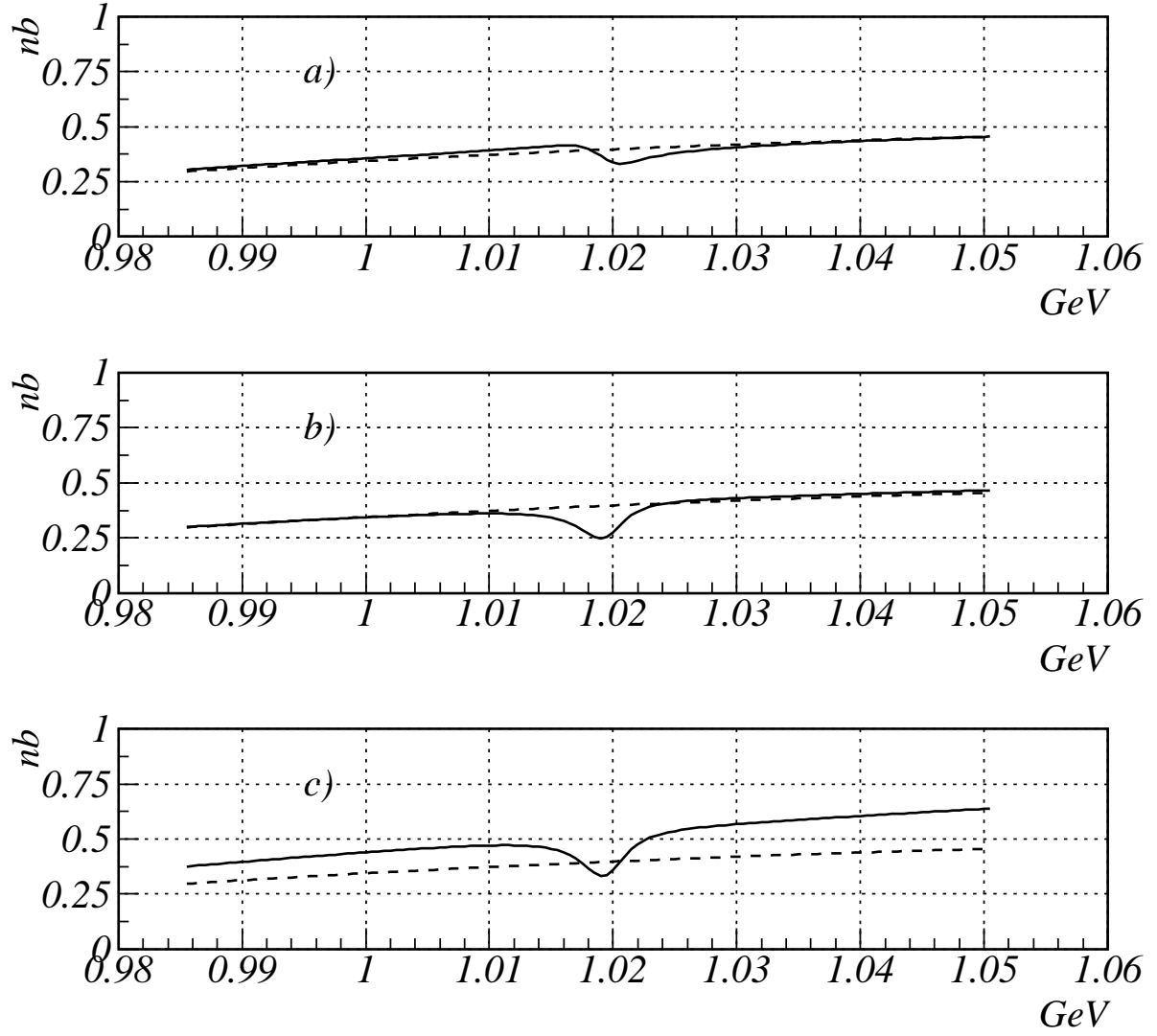


Figure 1: Theoretical predictions for  $\sigma(ee \rightarrow \omega\pi^0 \rightarrow \pi^0\pi^0\gamma)$ . Dashed line -  $\rho$ -meson contribution only. Solid line: a)  $\phi$ -meson contribution through  $\phi \rightarrow \rho\pi^0 \rightarrow \pi^0\pi^0\gamma$  is added. b)  $\phi \rightarrow \omega\pi^0$  transition due to  $\rho$ - $\omega$ - $\phi$  mixing is also included in the  $\phi$ -meson contribution. c)  $\rho'$ -meson contribution is added to the above ones.

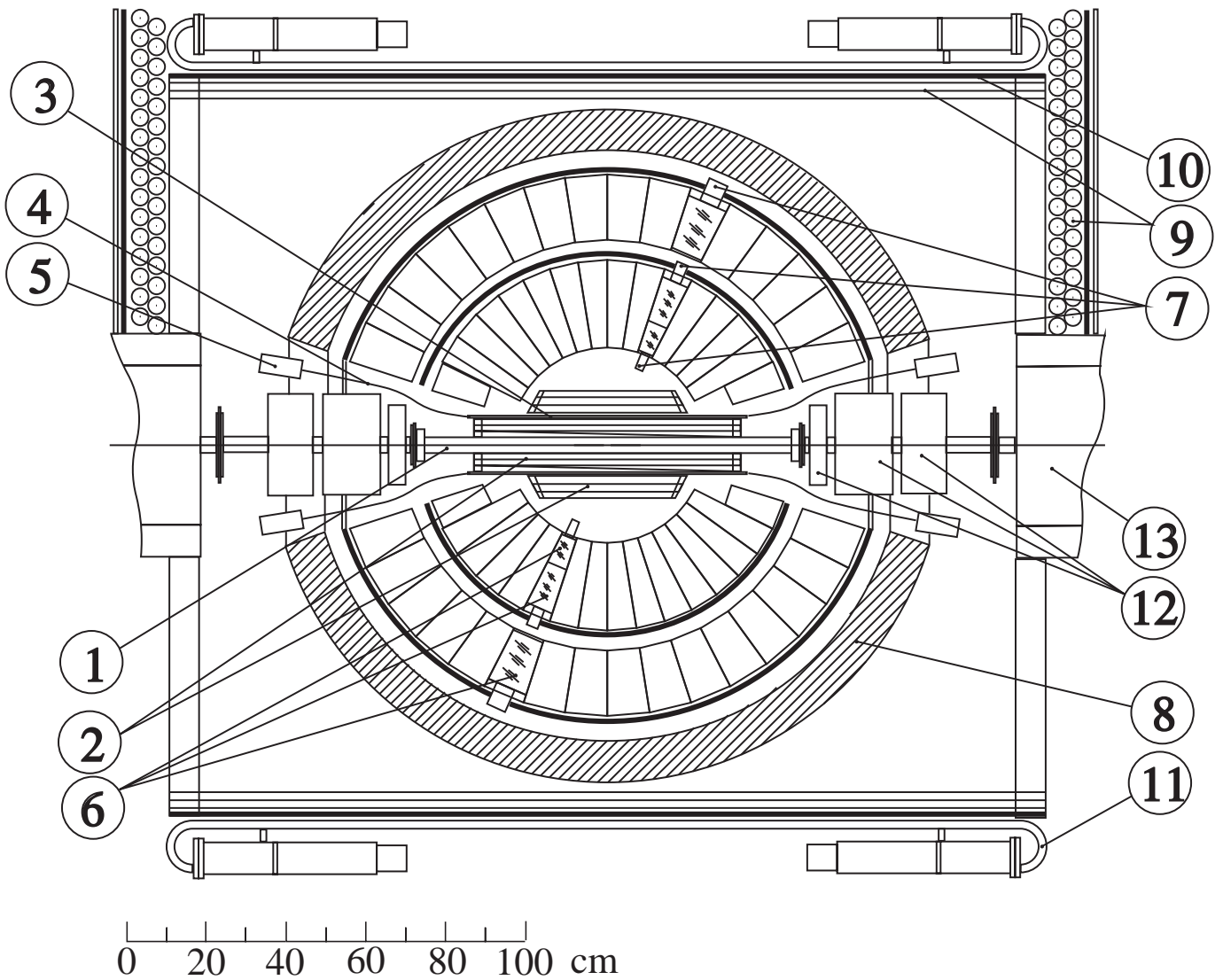


Figure 2: Detector SND — view along the beam; 1—beam pipe, 2—drift chambers, 3—scintillation counters, 4—fiber lightguides, 5—PMTs, 6—NaI(Tl) counters, 7—vacuum phototriodes, 8—iron absorber, 9—streamer tubes, 10—1 cm iron plates, 11—scintillation counters, 12—magnetic lenses, 13—bending magnets

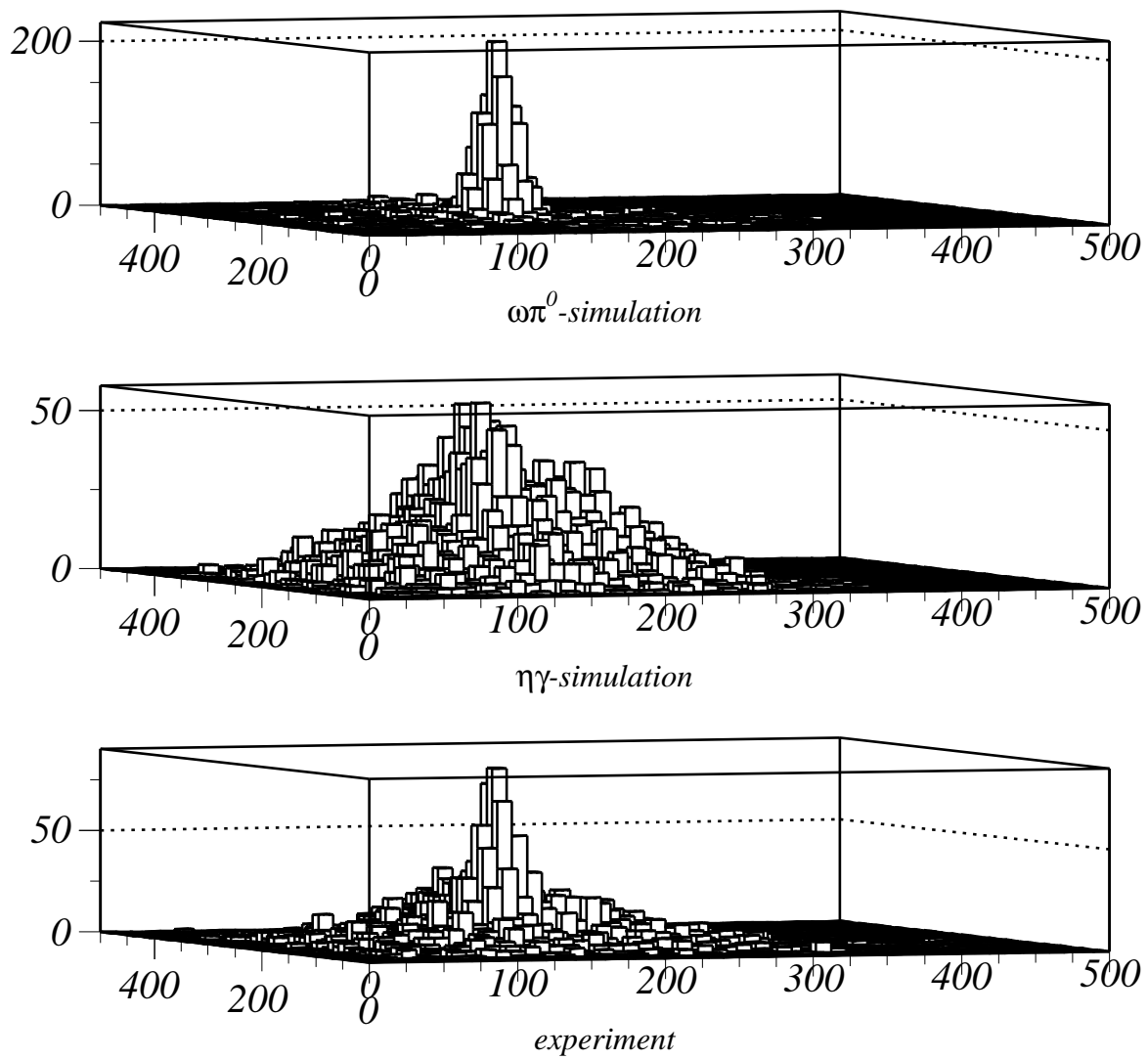


Figure 3: Distributions  $M_{24}$  versus  $M_{35}$  plus  $M_{25}$  versus  $M_{34}$  for MC simulation and experiment.

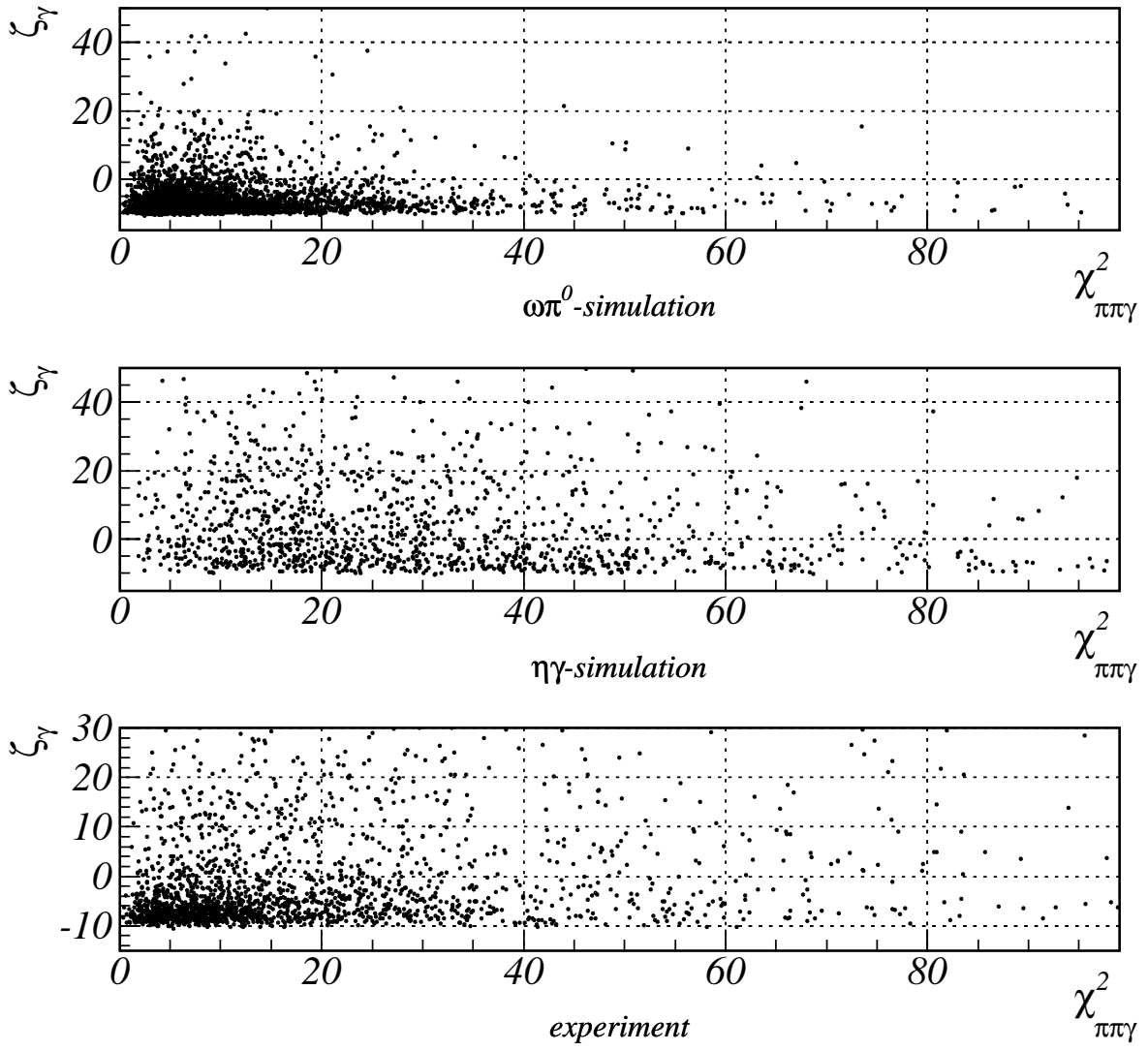


Figure 4:  $\zeta_\gamma$  versus  $\chi^2_{\pi^0\pi^0\gamma}$  distributions for MC simulation and experiment.

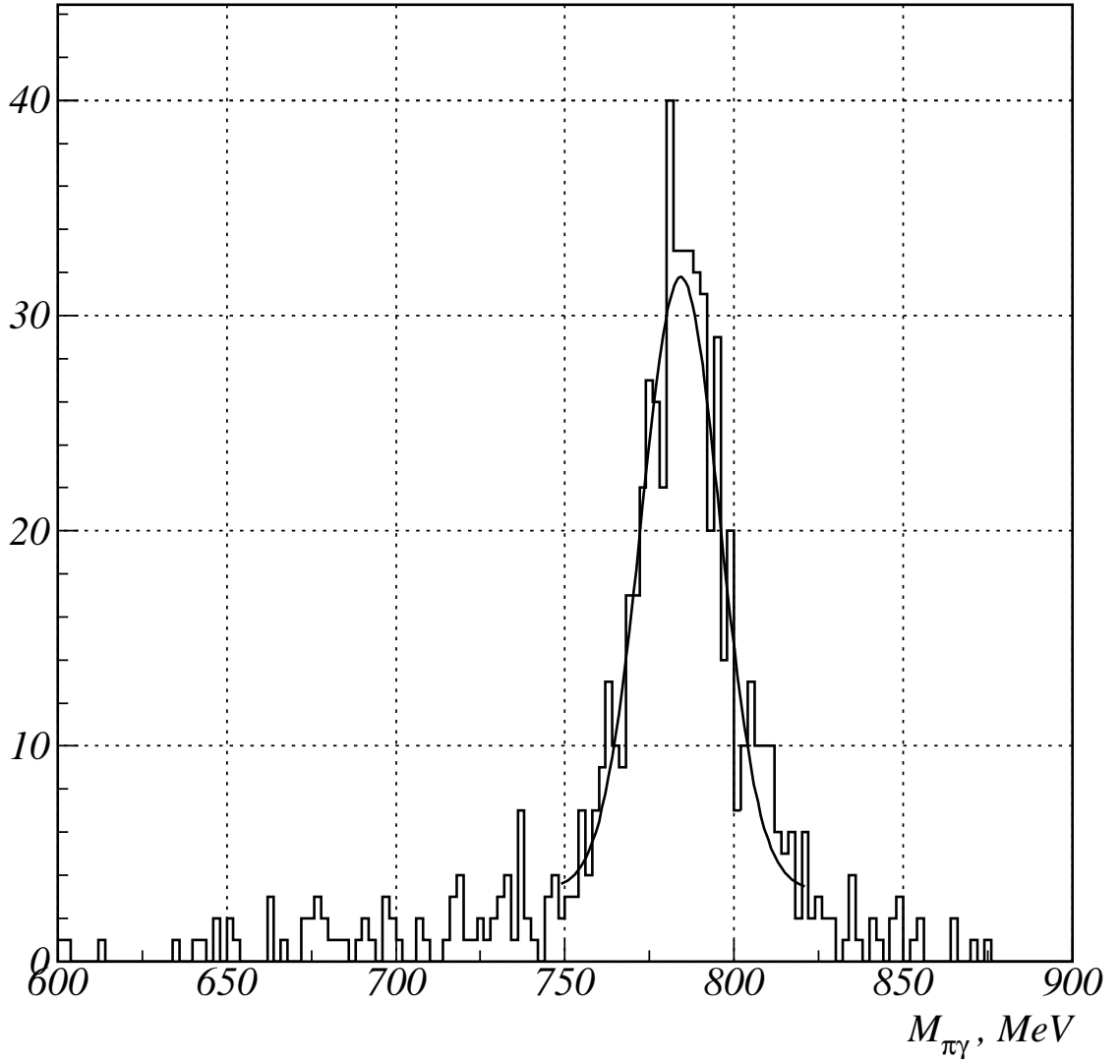


Figure 5:  $M_{\pi^0\gamma}$  (invariant mass of  $\pi^0\gamma$  nearest to  $\omega$ ) distribution for Cut I.



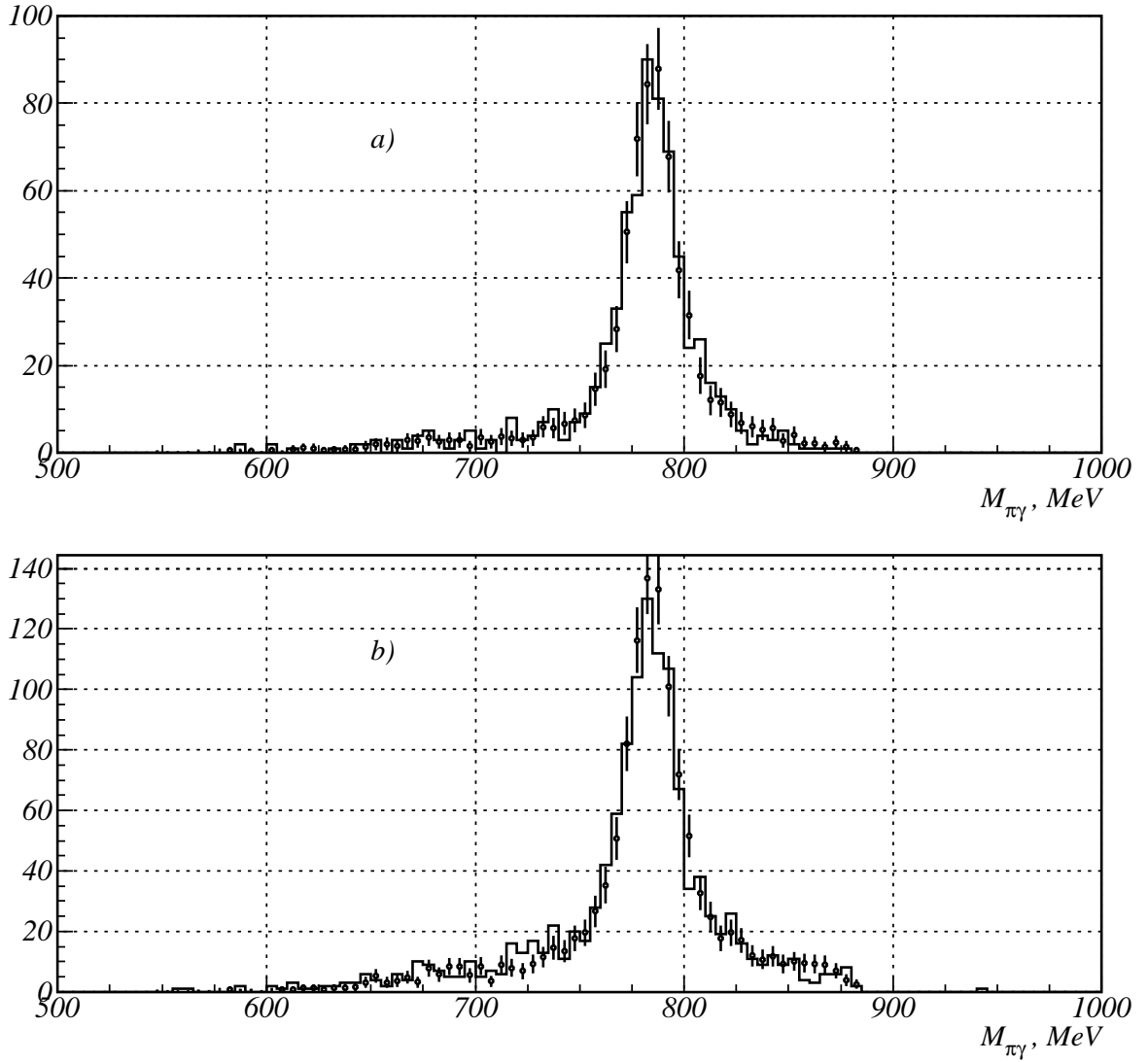


Figure 6:  $M_{\pi^0\gamma}$  distributions : MC simulation (points with error bars) and experiment (histogram). a) for Cut I, and b) for Cut II.

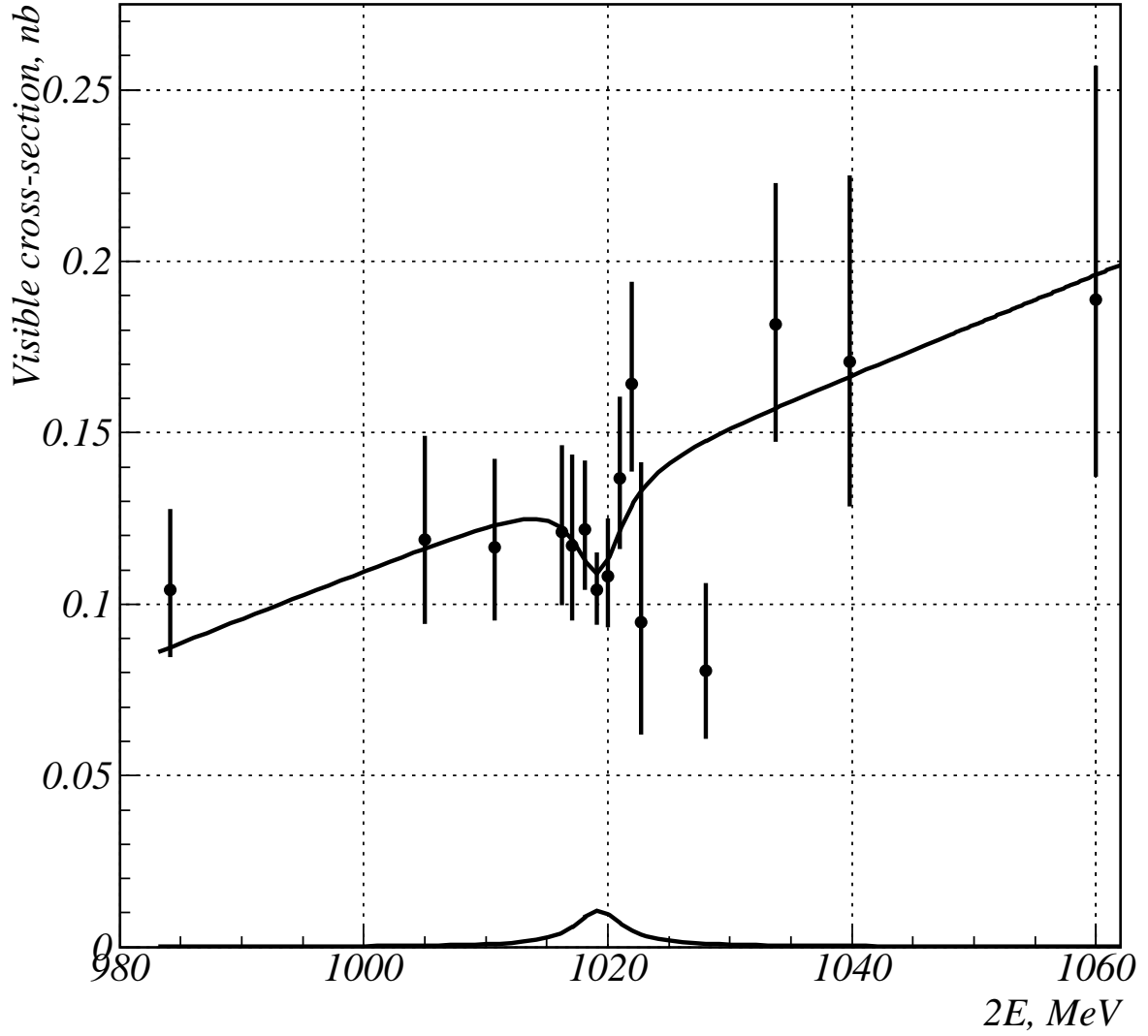


Figure 7: Detected cross-section for the process  $e^+e^- \rightarrow \omega\pi^0 \rightarrow \pi^0\pi^0\gamma$  under cuts of group 1 and optimal fit. The fitted resonant background is also shown at bottom.